JASS *Journal of Astronomy and Space Sciences*

Mesoscale Ionospheric Irregularity Oval at High Latitudes Observed by Global GNSS Networks (2010–2024)

Shun-Rong Zhang[†], Anthea J. Coster, Philip J. Erickson, Larisa P. Goncharenko, Jing Liu

Haystack Observatory, Massachusetts Institute of Technology, Westford, MA 01886, USA

This study investigates high-latitude ionospheric mesoscale irregularities associated with energetic particle precipitation and magnetosphere-ionosphere-thermosphere coupling processes within the auroral oval using ground-based Global Navigation Satellite Systems (GNSS) total electron content (TEC) measurements. This scale size is much larger than those associated with GNSS scintillations, which range from sub-kilometers (small scales) to > 10 km (large scales). Analyzing 15 yr of data from 2010 to 2024, we characterize, for the first time, the climatology of enhanced intensity of ionospheric mesoscale irregularities at high latitudes. The observed intensity of irregularities in GNSS TEC fluctuations can serve as a proxy for the dynamic behavior of the auroral oval which varies with magnetic local time, longitude, latitude, season, solar activity cycle, geomagnetic disturbances, and hemisphere. The spatial distribution of the irregularity is oval-shaped and therefore this pattern is named as "irregularity oval"; the morphology of the irregularity oval is generally aligned well with the known variations of auroral oval established by using other technologies. While the primary goal has been to document systematically these irregularity long-term observations, future work will focus on the development of a novel GNSS TEC-based "irregularity oval" model.

Keywords: Auroral oval, GNSS total electron content (TEC), mesoscale irregularity

1. INTRODUCTION

The auroral oval, a ring-shaped region encircling Earth's magnetic poles, signifies the upper-atmospheric footprint of charged particles from the solar wind and the magnetosphere that are guided along Earth's magnetic field lines. The oval is typically located between about 65° and 75° magnetic latitude under quiet geomagnetic conditions. There, these energetic particles collide with oxygen and nitrogen, emitting visible lights as aurora (Feldstein & Starkov 1967; Holzworth & Meng 1975; Evans 1986; Kivelson & Russell 1995; Ebihara & Ejiri 2000; Grocott et al. 2009). The auroral oval is maintained by magnetospheric convection driven by dayside reconnection and nightside substorms. The nightside portion of the oval is typically broader than the dayside, reflecting enhanced particle injection from the plasma sheet and expansion of the westward electrojet during substorm activity (Lockwood & Cowley 1993). Field-aligned currents (FACs) flow along closed, high-latitude magnetic field lines that map to the plasma sheet in the magnetotail and close through the auroral electrojet region in the ionosphere which forms the oval encircling the geomagnetic poles (Iijima & Potemra 1976).

The offset between the geographic and magnetic poles, along with the tilt of Earth's magnetic dipole, causes the auroral oval to appear asymmetrical in geographic coordinates but more circular in geomagnetic coordinates. However, asymmetry between day and night as well as dawn and dusk does exist in the magnetic coordinates.

The latitudinal span of the auroral zone depends on the radial distance in the plasma sheet, local time sector, and geomagnetic activity and solar wind and interplanetary magnetic field (IMF) conditions. In particular, on day side, particle precipitation comes from cusp and boundary layer sources, and the oval is typically narrower in latitude here. On nightside, more intense and broader auroral activity due to

plasma sheet injections and substorm equatorward expansion (Sergeev et al. 2012). At dawn/dusk sectors, asymmetries arise from the east–west electrojets and IMF By effects.

The precise location of the auroral oval can be determined using a combination of satellite-based imaging, ground-based optical observations, magnetometer arrays, in situ particle measurements, and other ionospheric measurements. Ultraviolet (UV) imagers onboard satellites such as POLAR, IMAGE, and DMSP provide global views of auroral emissions in the far-ultraviolet (FUV), enabling accurate mapping of the large-scale structure inside the oval (Frey et al. 2001; Zhang & Paxton 2008). Ground-based all-sky imaging (ASI) cameras offer high-resolution optical imagery of auroras in visible wavelengths (e.g., 557.7 and 630.0 nm), revealing fine-scale features and temporal evolution (Shiokawa et al. 1996; Donovan et al. 2006). Arrays of ground magnetometers, such as SuperMAG and IMAGE, track variations in horizontal magnetic fields to infer the strength and location of auroral electrojets, which align closely with the auroral oval (Gjerloev 2012). In situ particle detectors on satellites like DMSP and FAST measure precipitating energetic electrons and ions, directly identifying the boundaries of particle precipitation that define the auroral region (Newell et al. 1996). The THEMIS mission has significantly enhanced understanding of auroral dynamics by combining a constellation of satellites with ground-based ASIs and magnetometers, enabling direct observations of substorm onset and the temporal evolution of auroral structures (Angelopoulos 2008). The fluxgate magnetometer (FGM) onboard CHAMP provides extensive FAC density estimations which were used to develop a new auroral oval model, assuming the FAC enhancements occur within the oval (Xiong & Lühr 2014; Xiong et al. 2014). Additionally, high-latitude incoherent scatter radars (e.g., EISCAT, PFISR) detect ionospheric responses to auroral activity, such as enhanced electron densities and ion drifts (Nicolls & Heinselman 2007). These diverse measurements feed into empirical models, such as the OVATION Prime model, which statistically characterizes the location and intensity of auroras (Newell et al. 2014).

Global Navigation Satellite Systems (GNSS), such as GPS, GLONASS, and Galileo, have become powerful tools for auroral science, particularly in studying the ionospheric disturbances that accompany the auroral activity. When GNSS signals pass through the auroral ionosphere, they are affected by variations in electron density, especially during geomagnetic storms and substorms. Dual-frequency GNSS receivers are widely used to derive total electron content (TEC), which provides critical insights into electron density variations caused by particle precipitation, polar cap patches, subauroral ionospheric structures, and traveling ionospheric disturbances (Foster & Burke 2002; Foster et al. 2005; Zhang et al. 2013; Zou et al. 2014; Zhang et al. 2017a; Lyons et al. 2019; Zhang et al. 2019b; Nishimura et al. 2020; Zou et al. 2021; Zhang et al. 2022). Auroral processes also induce phase and amplitude scintillations of GNSS signals, making GNSS a powerful tool for detecting plasma irregularities and turbulence in the auroral ionosphere. The ionospheric irregularities can be monitored by using a GNSS index, ROTI (Rate of TEC Index change), as originally proposed by Pi et al. (1997) and now widely used for high, midlatitude, and equatorial science (Jakowski et al. 2012; Cherniak et al. 2014, 2018; Mrak et al. 2020; Sun et al. 2024). This index characterizes the intensity of the GNSS phase fluctuations caused by ionospheric irregularities. The present study, however, analyzed the mesoscale component of the TEC fluctuations, denoted as differential TEC (dTEC), to characterize the intensity of ionospheric irregularities inside the auroral over and polar cap region. The spatiotemporal scales of these irregularities are much larger than those associated with GNSS scintillations, ranging from sub-kilometers (small scales) to > 10 km (large scales). The dTEC method, which will be described in Section 2, has been widely utilized in the study of traveling ionospheric disturbances (TIDs; Saito et al. 1998) and ionospheric penetration electric field (Zhang et al. 2023). In the high-latitude region, dTEC could be related not only to TIDs, but also to ionization enhancement caused by sudden deposition of energetic particles, as well as to small intensity of plasma patches (Nishimura et al. 2020).

Global GNSS TEC data have been produced daily at Massachusetts Institute of Technology (MIT) Haystack Observatory since the start of widely scientific application of GPS data around 2000 and are archived in the Madrigal database (http://openmadrigal.org) for public use. Using these extensive GNSS data from 2010 to 2024, we explore the general climatology of mesoscale fluctuation levels of ionospheric electron density and establish their connection with the morphology and dynamics of the auroral oval.

2. DATA AND METHODS

MIT Haystack Observatory has developed the MAPGPS software suite to process GNSS observations, enabling the generation of global maps of TEC (Rideout & Coster 2006; Vierinen et al. 2016). The system currently utilizes data from over 6,000 global receivers contributed by community members, with a significant portion, exceeding 3,000, originating from the American sector. This extensive dataset comprises an astonishing 150 million line-of-sight (LOS)

segments every single day. These LOS data enable the daily determination of TEC fluctuations, which are calculated as differential TEC (dTEC). This continuous spatial-temporal coverage provides the necessary information for the systematic statistics presented here.

Ionospheric perturbation in TEC, dTEC, is obtained by detrending the smooth background vertical TEC variations using LOS slant TEC data from each individual pair of receiver-GNSS satellite. This general approach was initially proposed by Saito et al. (1998) and is now widely adopted by the community to study TIDs (Ding et al. 2007; Zakharenkova et al. 2016; Zhang et al. 2017b; Chou et al. 2018; Mrak et al. 2018; Inchin et al. 2023).

In the present study, the background vertical TEC is determined by using a low-pass filter (Savitzky & Golay 1964) with a linear basis function within a 30-minute sliding window (Coster et al. 2017; Zhang et al. 2017b, 2019a). The filter algorithm uses a convolution process with least squares fitting of successive subsets of windows of 30 minutes involving time-adjacent TEC data points from the same GNSS satellite-receiver pair and a linear basis function set. The 30-minute window is appropriate in detecting medium scale irregularities most effectively at midlatitudes or for structures moving below 300–400 m/s; but for high latitudes with convective speeds above 1,000 m/s, the scale size of the irregularities can be up to 2,000 km. A 15° cut-off elevation for receiver-satellite ray paths was used to eliminate data close to the horizon. Data at the start and the end of each continuous segment from the same GNSS satellite-receiver pair were disregarded to avoid potential "edge" effects (Zhang et al. 2019a, 2021), which arise because of lack of data in the 30-min window centering around the data edge. The dTEC accuracy is based on the GNSS phase measurement error, which is often less than 0.03 TEC unit (TECu, 1 TECu = 1×10^{16} el/m^2) (Coster et al. 2012), as all satellite and receiver bias terms cancel out in a differential sense. These dTEC values have been extensively used in studies related to TIDs such as those associated with solar eclipses, solar flares, solar terminator, geospace storms and substorms, volcanic eruptions, and lower atmospheric forcing (Zhang et al. 2017b; Lyons et al. 2019; Zhang et al. 2019a, b; Nishimura et al. 2020; England et al. 2021; Zhang et al. 2021, 2022; Chang et al. 2022; Lu et al. 2024; Tyska et al. 2024; Schmidt et al. 2025; Trop et al. 2025) and sudden global ionospheric disturbances associated with the penetration electric field (Zhang et al. 2023).

Fig. 1 provides some examples of TEC observations, the smooth background, as well as the fluctuation component (denoted as dTEC) along with GNSS satellite elevation and ionospheric pierce point information. The observations

in (a) and (b) came from stations underneath the auroral region during the 7 September 2017 intense geomagnetic storm, where fluctuations up to ± 1.5 TECu can be found in (a) and ± 4 TECu in (b). (c) and (d) were at higher latitudes where the clear oscillations in (c) are potentially related to TIDs on 7 September 2017 and the large density spikes of ~30 TECu in (d) were likely plasma patches on 10 October 2024.

It is important to note that the GNSS observations collected using the MIT TEC processing system have varying temporal resolutions. While a significant portion of the data has a sampling rate of 1 min, 1-sec sampling rate is also widely available. Therefore, we resampled the data with a standard rate of 15 sec through either resampling or linear interpolation. After this procedure, the data is subjected to filtering and detrending steps to calculate dTEC, as mentioned earlier. The final dTEC are resampled data with the original temporal resolution.

To characterize the intensity of irregularities, an additional binning step is taken in the present study. dTEC is binned into 1° longitude × 1° latitude × 5 min time bins. For each bin, an average value of |dTEC| (the absolute dTEC value), denoted as aTEC, is determined to represent the fluctuation intensity (amplitude). This bin size should be able to resolve the mean state of mesoscale fluctuations. The relative (percentage) intensity (amplitude) pTEC is defined as pTEC = aTEC/TEC, where TEC here is the bin average derived as for aTEC. The main focus of this study is to analyze these parameters at high latitudes during the period from 2010 to 2024. Fig. 2 shows TEC, aTEC, dTEC standard deviation, and pTEC obtained in the northern polar region at 0600 and 1800 UT during spring 2023. Combining data from the two UTs allows to piece together a full picture in the polar region. It is evident that aTEC and the standard deviation of dTEC exhibit similar characteristics: the dayside intense activity is bounded at ~75° apex latitudes, while the nightside intense activity is bounded at ~60°. Consequently, in our subsequent sections, we will use aTEC as proxy to quantify the intensity of irregularities.

3. RESULTS

In the following, we present the GNSS observational climatology of mesoscale irregularity at high latitudes presumably overlapping with the region of enhanced auroral activities. The aTEC averages over a given season or year as a function of UT or LT are calculated. To derive the seasonal averages from multiple-month data, daily observations are used for averaging, whereas for yearly
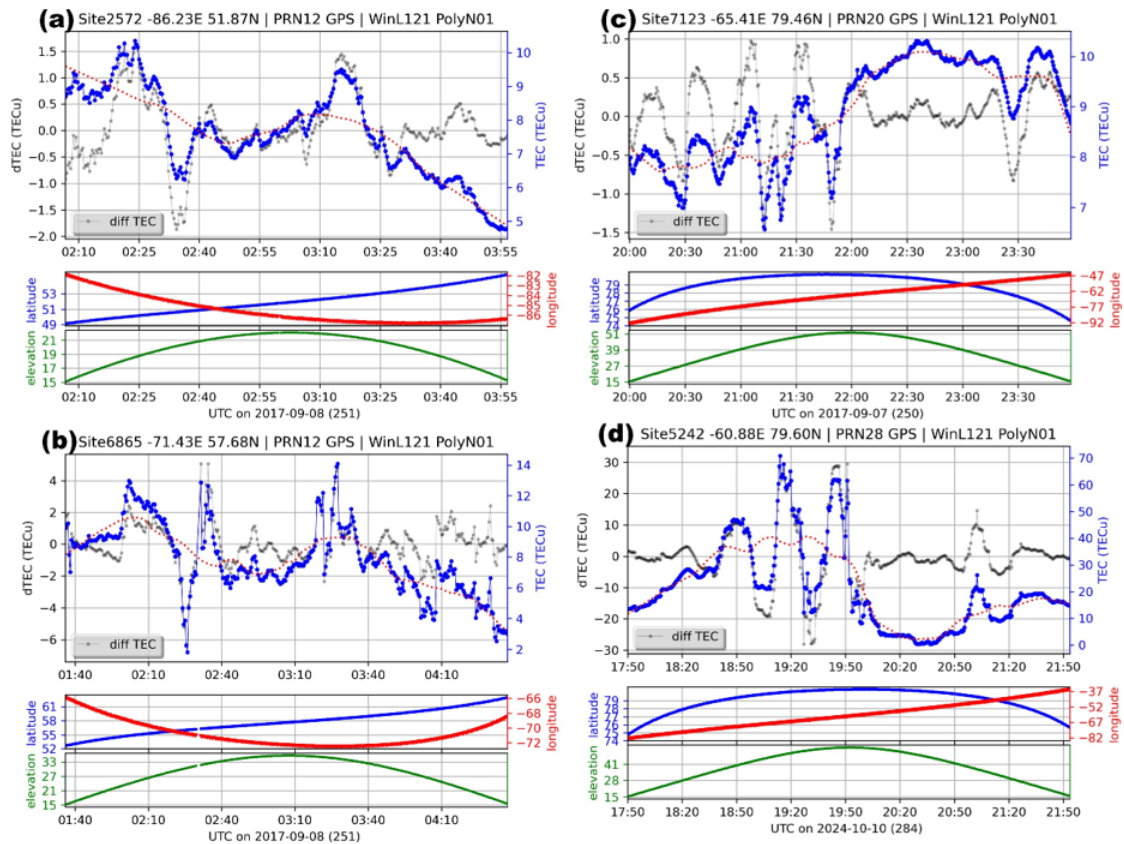
Fig. 1. GNSS line-of-sight TEC measurements. Sample vertical TEC data (blue line) from a specific LOS between each receiver–GNSS satellite pair, as well as the smooth background trend (red line) and the detrended component of TEC fluctuations (gray line), with IPP trajectory and satellite elevation information. (a) and (b) for the subauroral to auroral latitude span in the evening hours; (c) for the polar region in the afternoon with small (< 1 TECu) fluctuations; (d) for the polar region in the early afternoon with large density fluctuations (likely patches). TEC, total electron content; LOS, line-of-sight; GNSS, Global Navigation Satellite Systems; IPP, ionospheric pierce point.

Fig. 2. Polar region GNSS TEC parameters. Polar view of GNSS ionospheric observations in the northern hemisphere at 06 UT (top panels) and 18 UT (bottom panels) as seasonal averages during spring 2023 for TEC (in TECu, column 1), the dTEC absolute value denoted as aTEC (in TECu, column 2), dTEC standard deviation (in TECu, column 3), and the dTEC absolute value in percentage fraction denoted as pTEC (column 4). Black light lines are Apex iso-latitudes up to 75° at 15° interval. The shadowed region stands for the nightside. GNSS, Global Navigation Satellite Systems; TEC, total electron content.

averages, only 10-quietest days in each month are used for averaging. Section 3.4 on geomagnetic disturbance effects and Section 3.5 on solar cycle dependence show results of grouping according to the geomagnetic activity.

3.1 UT and LT Time-Dependent Variations

Polar views for a given UT provide snapshots of high-latitude longitudinal and latitudinal variations. Figs. 3 and 4 show yearly average patterns of UT-dependent aTEC
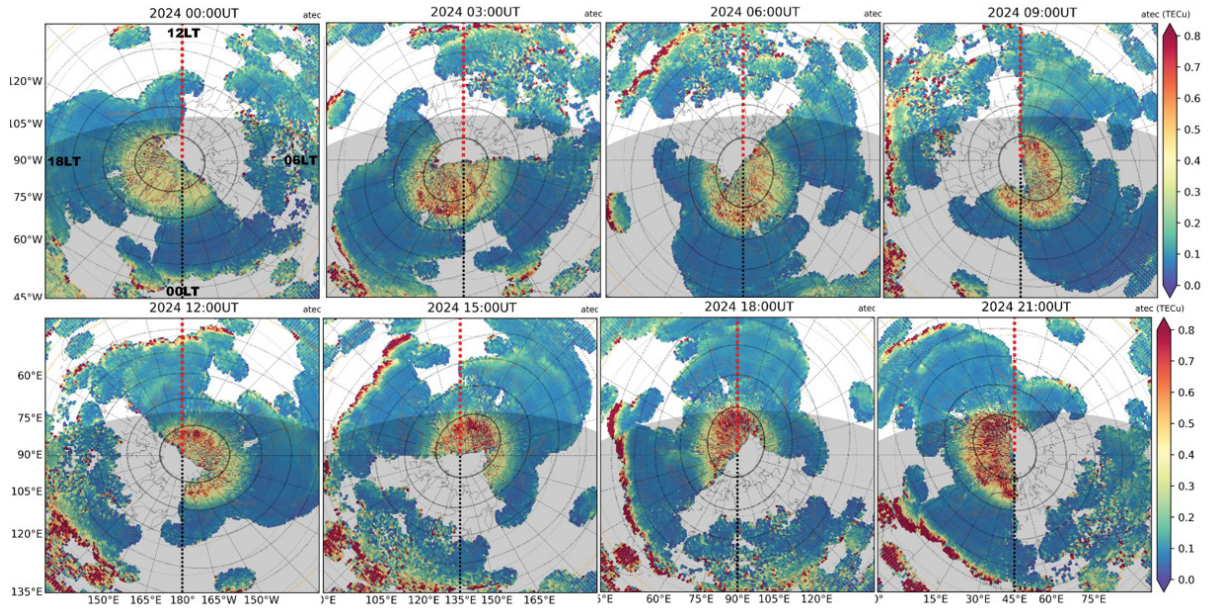

Fig. 3. Irregularity intensity UT dependency for 2024. Polar region aTEC patterns at different UTs as yearly averages for a high solar activity year of 2024 (excluding "international 5 most disturbed days"). The shadowed region stands for the nightside in winter and the red and black dashed lines represent local noon and midnight, respectively. TEC, total electron content.
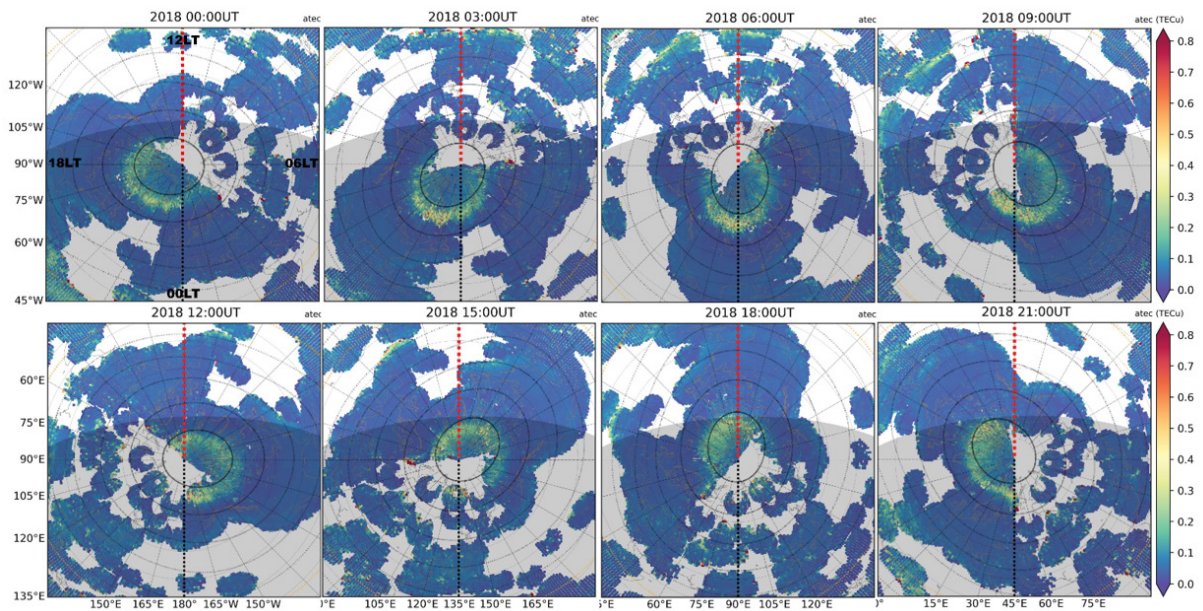

Fig. 4. Irregularity intensity UT dependency for 2018. Polar region aTEC patterns at different UTs as yearly averages for a low solar activity year of 2018 (excluding "international 5 most disturbed days"). The shadowed region stands for the nightside in winter and the red and black dashed lines represent local noon and midnight, respectively. TEC, total electron content.

variations in the northern hemisphere for 2024 and 2018, respectively.

In 2024, the large aTEC (≥ 0.4 TECu) occurs within the general area of apex latitude ≥ 60°N, being closer to ≥ 75°N on dayside and extended toward ~65°N on nightside. However, some of the largest aTEC is observed near apex latitudes 67°N–68°N on nightside (0.7 TECu at 03 UT and 21 UT) and ~80°N on dayside (0.75 TECu at 15 UT and 18 UT). The dayside aTEC is generally larger than on the nightside. In 2018 during very low solar activity, however, the location of aTEC enhancement zone is similar to that in 2024, though the aTEC is generally smaller in 2018 than in 2024.

LT-dependence can be identified from Figs. 5 and 6. From 03–12 LT, the enhancement zone moves from apex latitude
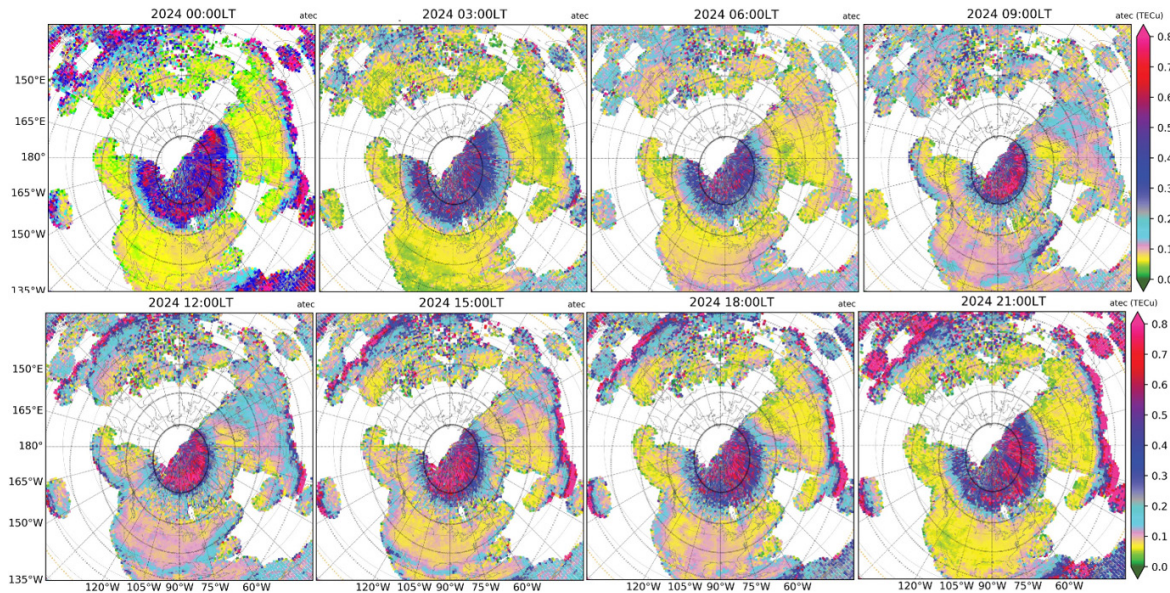

Fig. 5. Irregularity intensity local time dependency for 2024. Polar region aTEC patterns at different LTs as yearly averages for a high solar activity year of 2024 (excluding "international 5 most disturbed days"). The shadowed region stands for the nightside in winter and the red and black dashed lines represent local noon and midnight, respectively. TEC, total electron content.
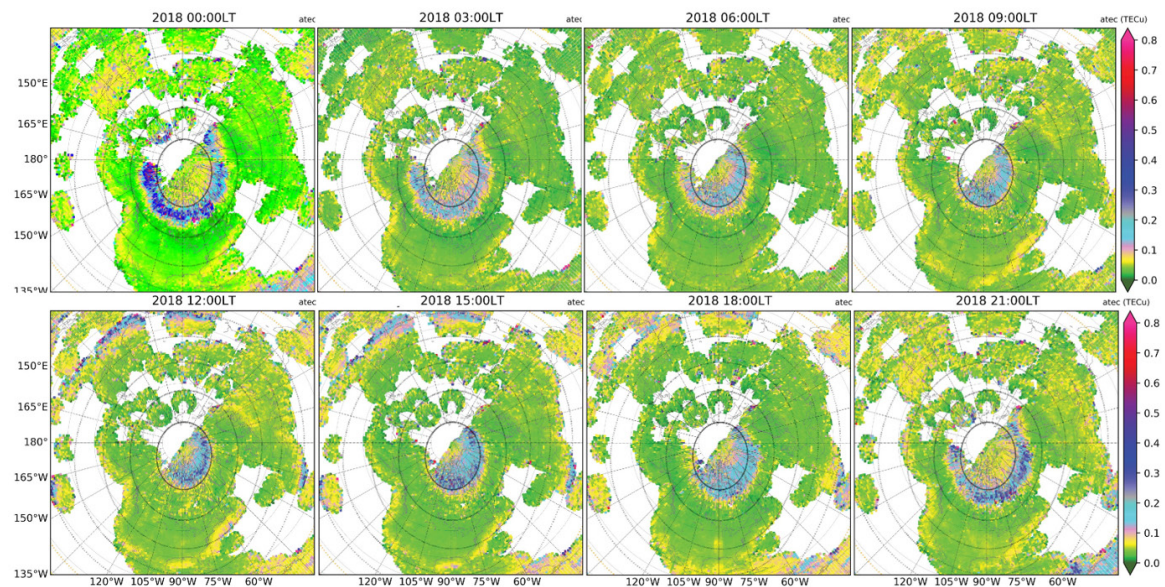

Fig. 6. Irregularity intensity local time dependency for 2018. Polar region aTEC patterns at different LTs as yearly averages for a low solar activity year of 2018 (excluding "international 5 most disturbed days"). The shadowed region stands for the nightside in winter and the red and black dashed lines represent local noon and midnight, respectively. TEC, total electron content.

65°N toward 70°N, and from 12–21 LT, it moves backwards toward lower latitudes. The same trends are developed in both low and high solar activity years 2024 and 2018, however, inside the polar cap, the enhancements during daytime hours are more evident in the high solar activity year 2024 (~0.7 TECu) than in the low solar activity year 2018 (~0.4 TECu). The nightside enhancement zones are wider in local time sectors close to the midnight for both solar activity levels.

While the exact reasons for high aTEC values on the dayside and during high solar activity years remain an important question for future studies, it is worth noting the following factors: (1) the energetic particles flux can be more intense as a result of dayside reconnection; (2) the proton precipitation more likely on dayside carries more energy; (3) the magnetic field geometry can influence the precipitation efficiency; and (4) the higher conductivity on dayside and during high solar activity years can modify the magnetosphere-ionosphere coupling.

3.2 Seasonal Dependency

To evaluate the seasonal dependency of aTEC, 3-month averages centering on the equinox and solstice months, respectively, are obtained and shown in Figs. 7 and 8 for the high solar activity years between 2022–2023.

In Fig. 7, results for 06 and 18 UT provide complementary spatial coverage on both dayside and nightside. On nightside (as shown for 06 UT), although the aTEC intensity is consistently strong above apex latitude 65°N, equinox seasons exhibit higher intensities (0.7–0.75 TECu), whereas solstice seasons exhibit much weaker aTEC intensities (0.4–0.6 TECu). On the dayside (as shown for 18 UT), while aTEC intensification is consistently confined to above apex latitude 68°N, aTEC shows intensification only in the narrow noon sector at ~0.65 TECu levels in summer and fairly so in autumn. Interestingly, in these two seasons of low intensity of irregularities, at 18 UT, the 75° apex latitude circle is entirely sunlit with large background ionospheric density.

The midnight and noon results are further compared in Fig. 8. Again, equinox seasons are characterized with higher intensity, particularly on nightside within the auroral oval and into the polar cap, with the low latitude boundary being more equatorward. Winter and summer solstices exhibit smaller aTEC. One possible explanation for the high aTEC in equinox is the stronger geomagnetic disturbance as the IMF projection onto Earth's field lines maximizes the Bz component (Russell & McPherron 1973). On dayside, while high aTEC in equinox confines to apex latitudes > 75°N, aTEC in winter appears abnormally high. This winter dayside feature remains an interesting scientific topic for further research to clarify whether the low ionospheric conductivity leads to stronger energetic particle precipitation.

3.3 Hemispheric Differences

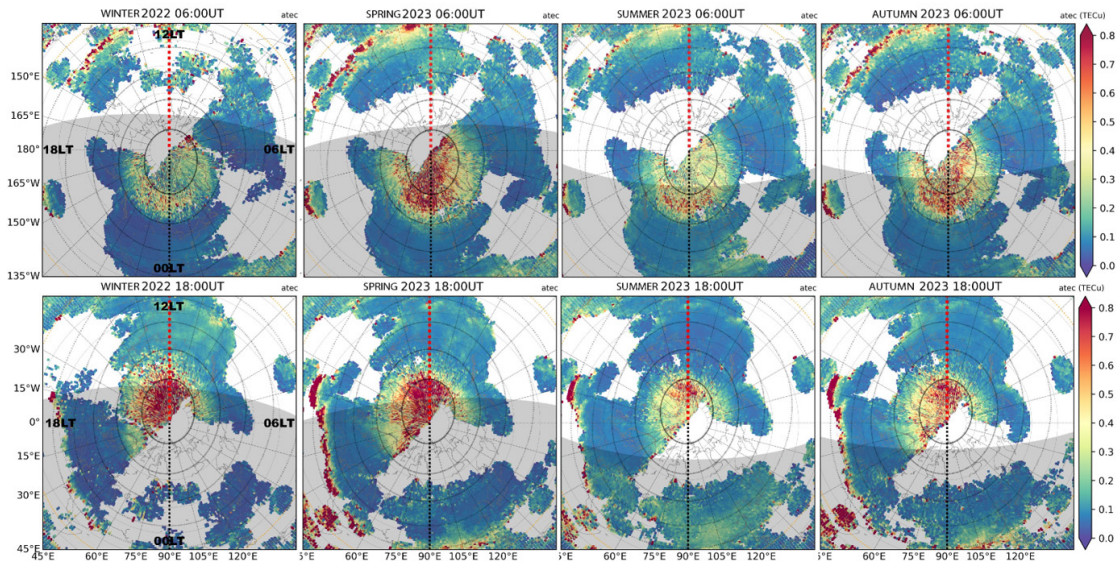Hemispheric differences in the aTEC intensity can be

Fig. 7. Irregularity intensity seasonal dependency for different UTs. Polar aTEC patterns as seasonal averages from winter 2022 to autumn 2023 at 06 and 18 UT. Each season uses 3-month' worth of observations for averaging. Note the terminator is shown for the beginning month of the 3-month seasonal bin (e.g., November for winter, February for spring, May for summer, and August for autumn). TEC, total electron content.
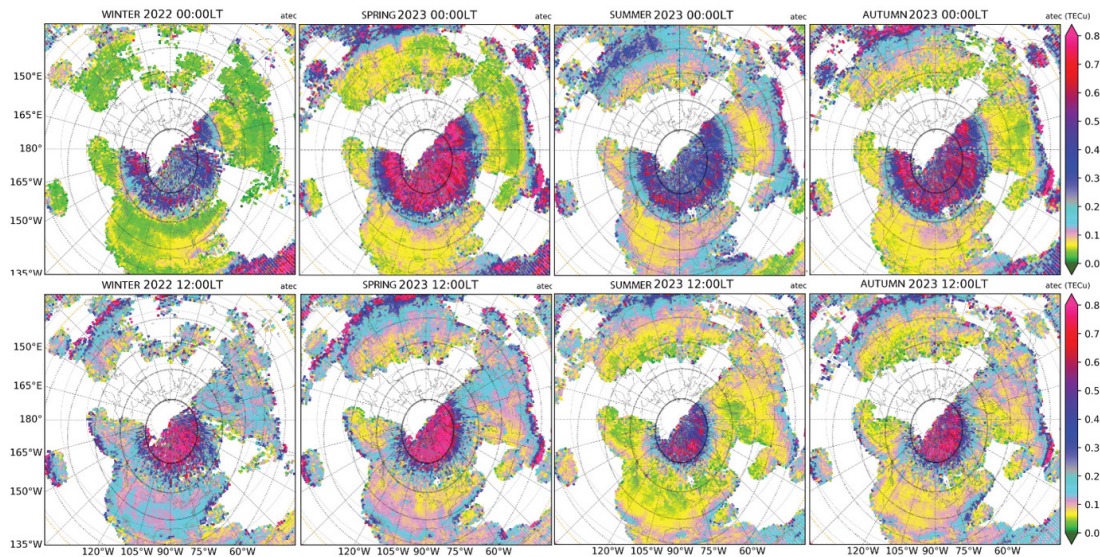
Fig. 8. Irregularity intensity seasonal dependency for midday and midnight. Polar aTEC patterns as seasonal averages from winter 2022 to autumn 2023 at 00 and 12 LT. Each season uses 3-month' worth of observations for averaging. Note the terminator is shown for the beginning month of the 3-month seasonal bin (e.g., November for winter, February for spring, May for summer, and August for autumn). TEC, total electron content.

observed according to LT. Fig. 9 shows these results as yearly averages for 2018 and 2024 with dramatically different solar activity levels. Although large data gaps in the southern hemisphere, general auroral oval can still be identified. The band of enhanced aTEC area is organized based on apex magnetic latitudes, with the midnight band being 10° wide starting at apex 65°N/S, and the midday band starting at apex 75°N/S. The main differences, however, lie in the aTEC intensity. At midnight, the northern hemispheric intensity in the auroral oval is considerably higher, whereas at noon, the northern hemispheric intensity in the cusp region is weaker. This is the case in both low and high solar activity years, and in the low solar activity year 2018 it is more evident.

3.4 Geomagnetic Disturbance Effects

Our statistical analysis has used all of the everyday observations in Figs 2, 7, and 8 to calculate *s*easonal averages, but only "international 10 quietest days" in each month in Figs. 3–6, and 9 to calculate *y*early averages. In this section, we compare results obtained during "international 10 quietest days" (hereafter "quiet days") and "international 5 most disturbed days" (hereafter "disturbed days").

Fig. 10 demonstrates such geomagnetic disturbance effects for spring 2023 as a function of UT and LT. The results obtained on those quiet days indicate GNSS TEC responses to a background precipitation effect, which likely includes the diffuse aurora caused by wave-particle scattering in the plasma sheet, as well as other processes. These responses

require a dedicated analysis. The low-latitude boundary of the auroral oval represented by aTEC activity during quiet days is confined to higher apex magnetic latitudes, being 2°–3° higher in latitude than that during disturbed days, and the intensity enhancement in aTEC during quiet days is clearly weaker and occurs more likely at higher latitudes. The high-latitude boundary of the auroral oval as seen in aTEC moves also poleward during disturbed conditions. Overall, the entire oval is expanded and activities are intensified during disturbed days. This feature will be further demonstrated in Figs. 11 and 12.

3.5 Solar Cycle and Yearly Dependency

We now use observational monthly averages to demonstrate the dependency on solar cycle in the aTEC latitudinal variation at noon and midnight, respectively. These averages are calculated for the entire month (i.e., including disturbed days) and are used for comparisons with those during quiet days.

As depicted in Fig. 11 (noon) and 12 (midnight), (1) the intensity of irregularities represented by aTEC during high solar activity is higher at noon than at midnight; during low solar activity, however, aTEC is weaker at noon (< 0.3 TECu) than at midnight (> 0.4 TECu); (2) at noon, the low- latitude boundary of the intensity enhancement is influenced significantly by solar activity, reaching a low latitude limit of 60°N (geographic) in Jan 2015, a low latitude limit of 70°N (geographic) in Jan 2020, and then back to 60°N again around Jan 2024; (3) during quiet days, this noontime low-
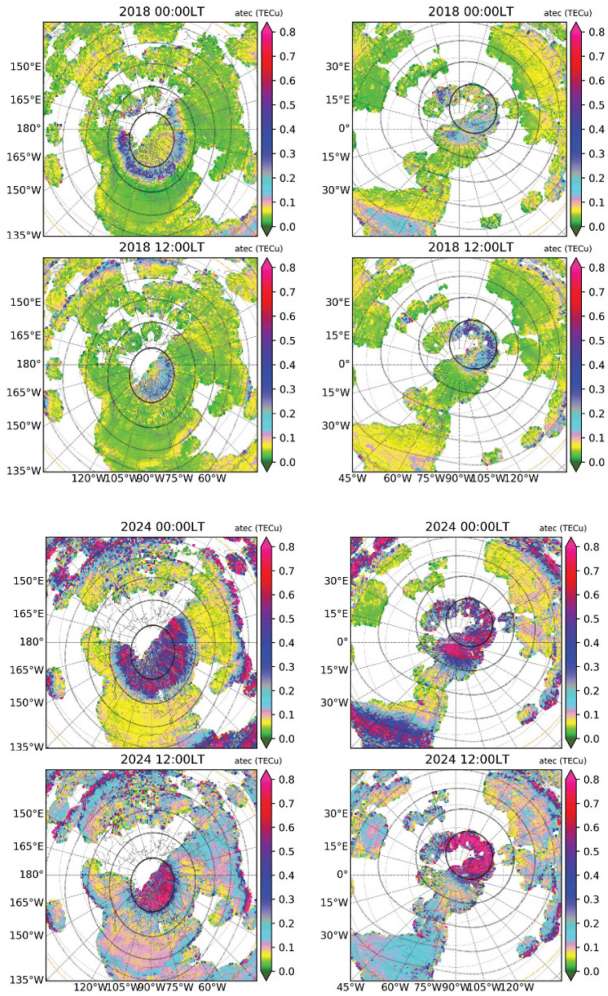
Fig. 9. Northern (left panel) and southern (right panel) hemispheric comparisons at given local times 00 LT and 12 LT for 2018 and 2024.

latitude limit varies with solar activity, following the same trend as described in (2), but the intensity of irregularities is significantly weaker for these quiet days as indicated in Section 3.4; (4) at midnight, the band of intensity enhancement within the auroral oval varies depending on the solar cycle. During high solar activity, the band is wider with its lower latitude limit extending equatorward, and during low solar activity, the band is narrower with its lower latitude limit retreating poleward; (5) during quiet days, this midnight band is much narrower with reduced intensity of irregularities (from > 0.4 TECu to < 0.4 TECu on average) within it; (6) the high-latitude limit of enhanced irregularity intensity is extended into the entire polar cap on both dayside and nightside during high solar activity, whereas during low solar activity, the irregularity oval has a much narrow latitudinal span.

The feature (6) mentioned above indicated that the

intensity of mesoscale irregularities has significantly increased throughout the polar cap. As discussed in the subsequent Section, this feature is likely associated with electron density structures, such as transpolar TIDs, tongue of ionization (TOI), and polar cap patches with varying spatial sizes. These are formed during IMF Bz fluctuations and other conditions.

Full northern polar views are also shown in Fig. 13 (noon) and in Fig. 14 (midnight) throughout the period of 2010–2024 as yearly averages during quiet days. The solar cycle dependence of intensity of irregularities and the width of the auroral oval, which are all organized along apex latitude, is significant. Figs. 15 and 16 shows these polar maps at 06 UT and 12 UT. These UT maps show not only the intensity enhancement (auroral) locations at noon and midnight but also other local times, demonstrating the curvature changes into elliptical oval between midnight and noon.

4. DISCUSSION AND SUMMARY

This study examines ionospheric mesoscale irregularities at high latitudes, specifically those caused by energetic particle impacts on the ionospheric electron density and magnetosphere-ionosphere-thermosphere coupling processes within the auroral oval. The intensity of mesoscale irregularities is determined by using GNSS TEC observations with the TEC fluctuation component being extracted and evaluated within 1° longitude × 1° latitude × 5 min time bins. Global GNSS TEC measurements over a 15-yr period, spanning from 2010 to 2024, provide very extensive data for this analysis, resulting in a comprehensive and reliable meso-scale irregularity climatology at high latitudes.

The spatial distribution and variability of the intensity of irregularities are essentially overlapped with the auroral oval, thus the "irregularity oval" can serve as a reasonable proxy to represent the auroral oval dynamics, influenced by various factors such as local time/longitude, latitude, season, hemisphere, magnetic disturbance, and the solar cycle. Specifically, (a) the "irregularity oval" has its low latitude limit at midnight being low than at noon, and expanded equatorward during enhanced geomagnetic activity and solar activity; (b) The intensity of the irregularities appears strong on dayside than on nightside during high solar activity, and strong on nightside than on dayside during low solar activity; (c) the nightside intensity is strong in equinox than in solstices, and in summer than in winter; however, the dayside intensity is high in winter and weak in summer; and (d) during low solar activity, the intensity enhancement occurs only within the "irregularity oval" on both dayside
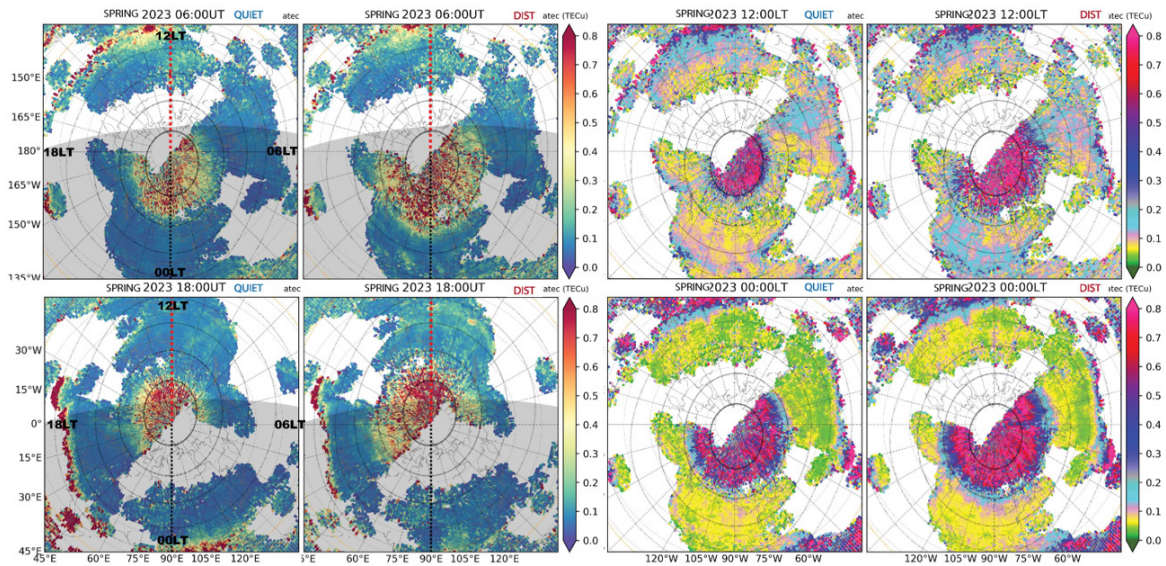
Fig. 10. A comparison of average patterns during geomagnetic quiet and disturbance days. Left two columns are for 06 UT (top) and 18 UT (bottom) during quiet days (left) and disturbed days (right). The right two columns are the same as the left two except for 12 LT and 00 LT.
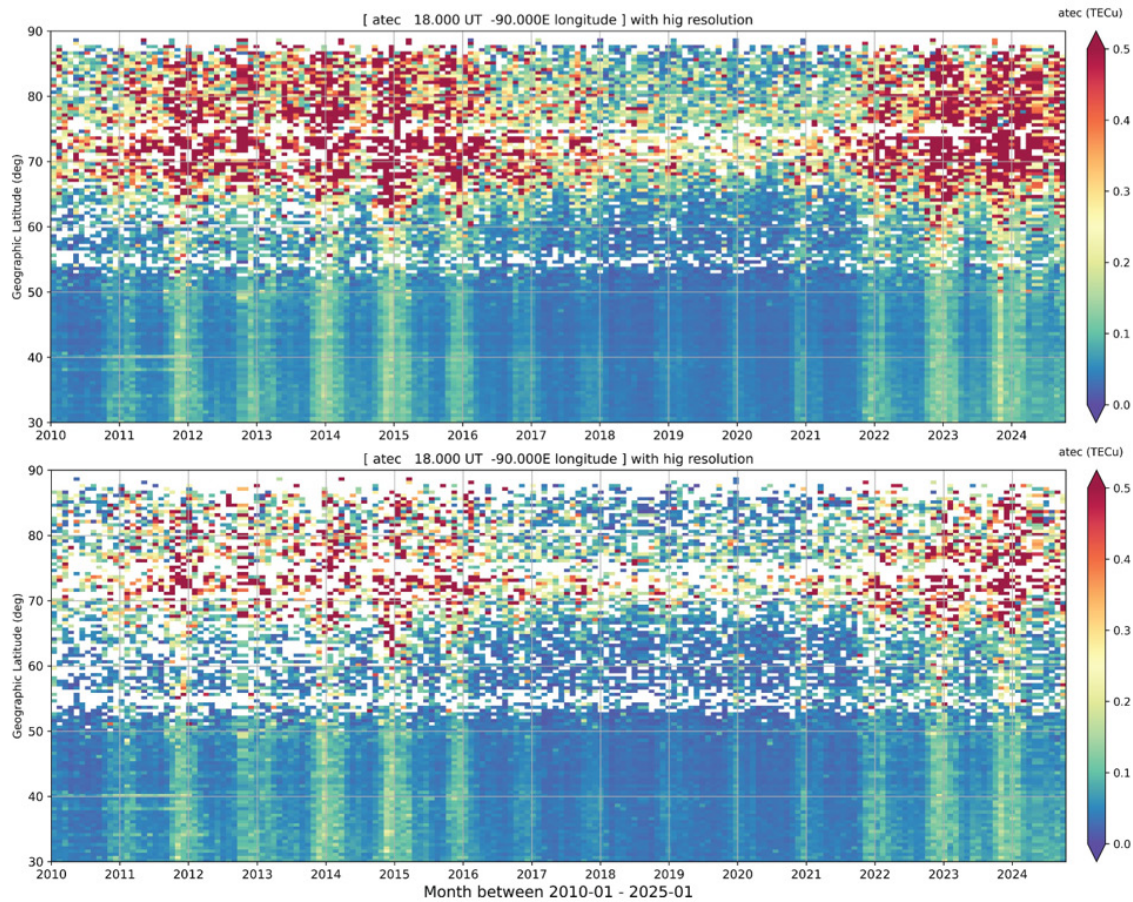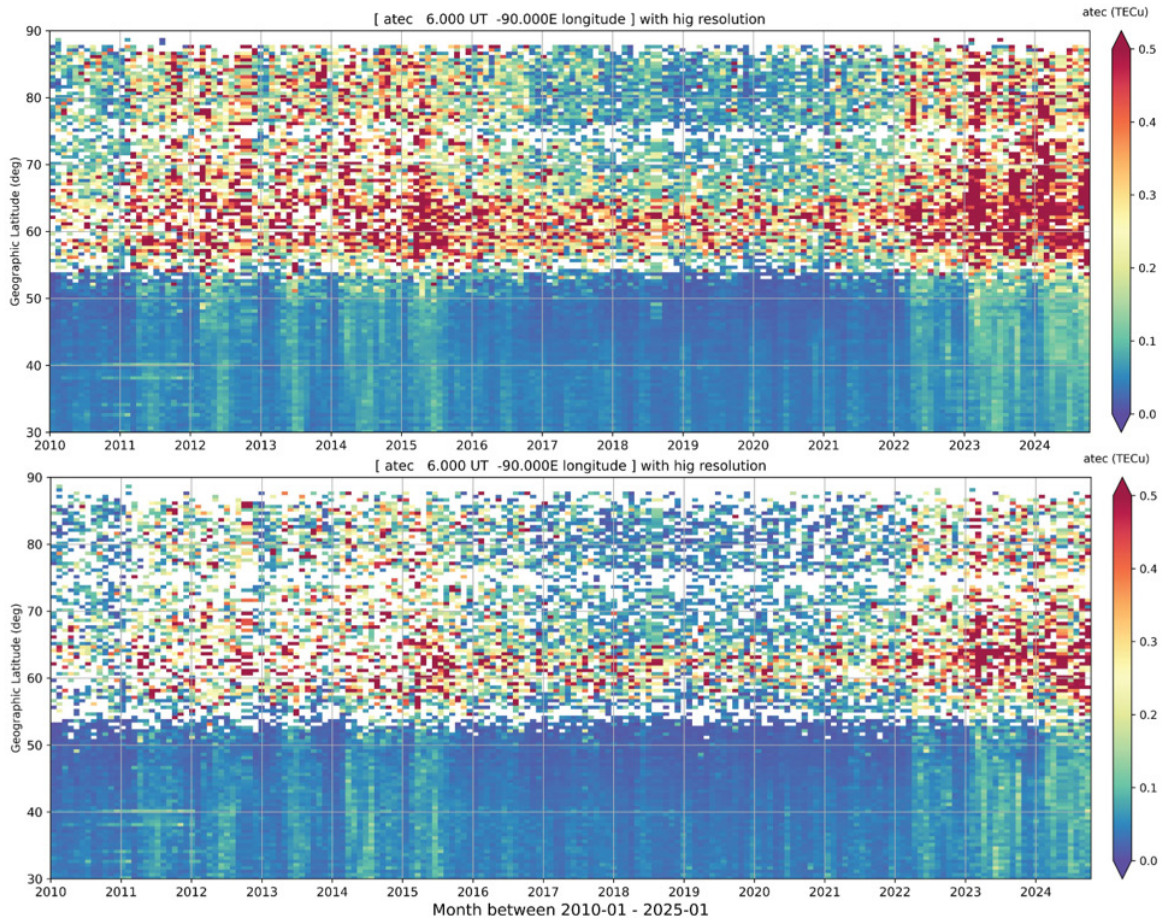

Fig. 11. Month-by-month latitudinal variations of aTEC around −90°E at 1800 UT (12 LT) derived every day in a month (upper panel) and during the international 10 most quiet days (bottom panel). TEC, total electron content.

Fig. 12. Month-by-month latitudinal variations of aTEC around –90°E at 0600 UT (00 LT) derived every day in a month (upper panel) and during the international 10 most quiet days (bottom panel). TEC, total electron content.

and nightside, whereas during high solar activity, the entire polar cap throughout dayside and nightside experiences the enhanced intensity of irregularities.

The observed mesoscale irregularities represent ionospheric density structuring inside the auroral oval. While identifying the exact causes of the variability and climatology of these irregularities needs information beyond the intensity measurements, as shown here, some essential processes may be speculated. (1) Particle precipitation induced impact ionization that can influence both the E and F regions. Those associated with diffusion aurora and soft particle precipitation may lead to the F-region mesoscale irregularity. With enhanced substorm activities, the auroral zone is moved equatorward, and the auroral E may be responsible for the elevated intensity of irregularities. (2) TIDs inside the aurora and adjacent areas may be excited. LSTIDS are often observed following the Joule heating enhancement, which excites GWs in the neutral atmosphere that propagate away from the heating region into lower and

higher latitudes. Some LSTIDs that propagate meridionally may constitute those mesoscale irregularities. MSTIDs has been reported to occur at subauroral latitudes arising from ionospheric instabilities due to enhanced storm-time electric field (Zhang et al. 2022; Sato et al. 2024). It is not clear how frequently these TIDs occur and what form they may take inside the auroral region. Additionally, transpolar TIDs have often been observed to travel from the dayside to nightside through the polar cap (Zhang et al. 2019b; Nishimura et al. 2020). (3) Other plasma density gradient structures, including patches and Tongue of Ionization, are also possible sources of observed density irregularities. These structures may not be precisely mesoscale any more but contribute to the observed irregularities. These can be intensified during solar wind and geomagnetic disturbances and can be observed inside the auroral oval as well as in the polar cap.

While the primary objective of this study has been to systematically document the climatology of ionospheric
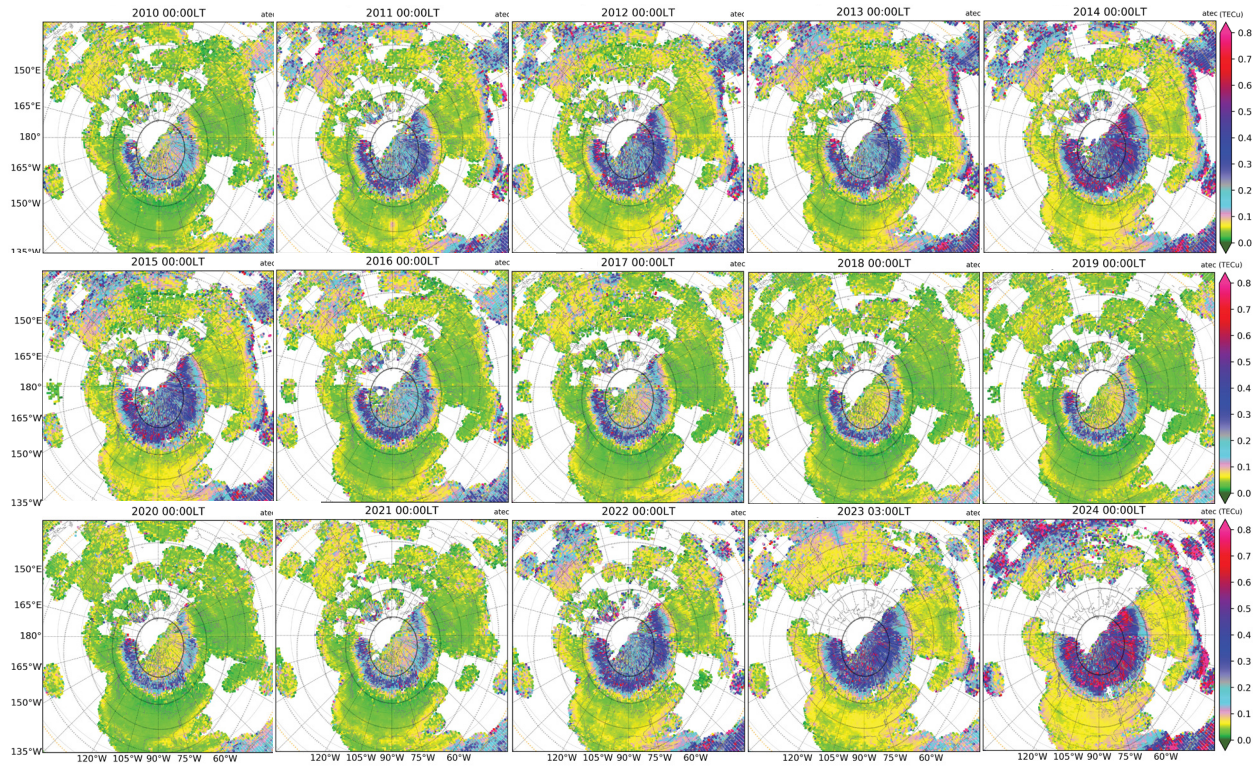
Fig. 13. Northern polar maps at 00 LT as yearly averages for 15 yr from 2010–2024 during those international 10 most quiet days each month.
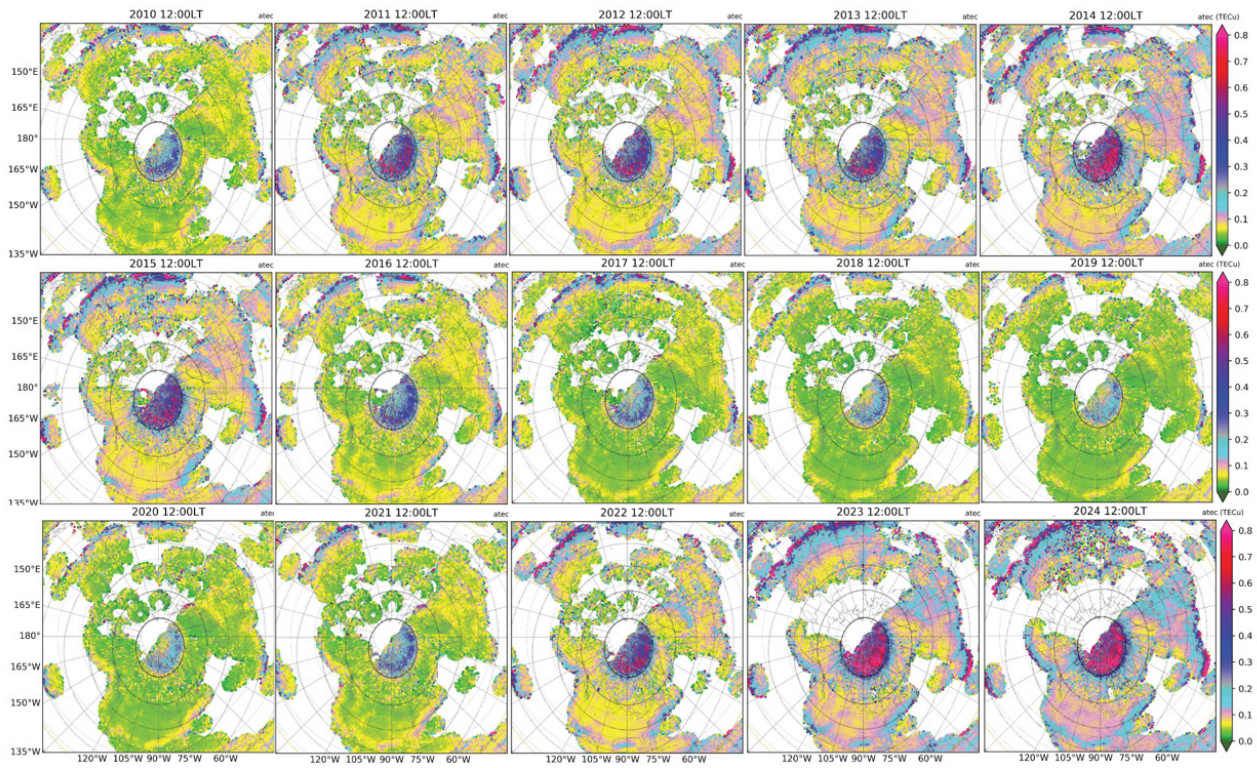

Fig. 14. Northern polar maps at 12 LT as yearly averages for 15 yr from 2010–2024 during those international 10 most quiet days each month.
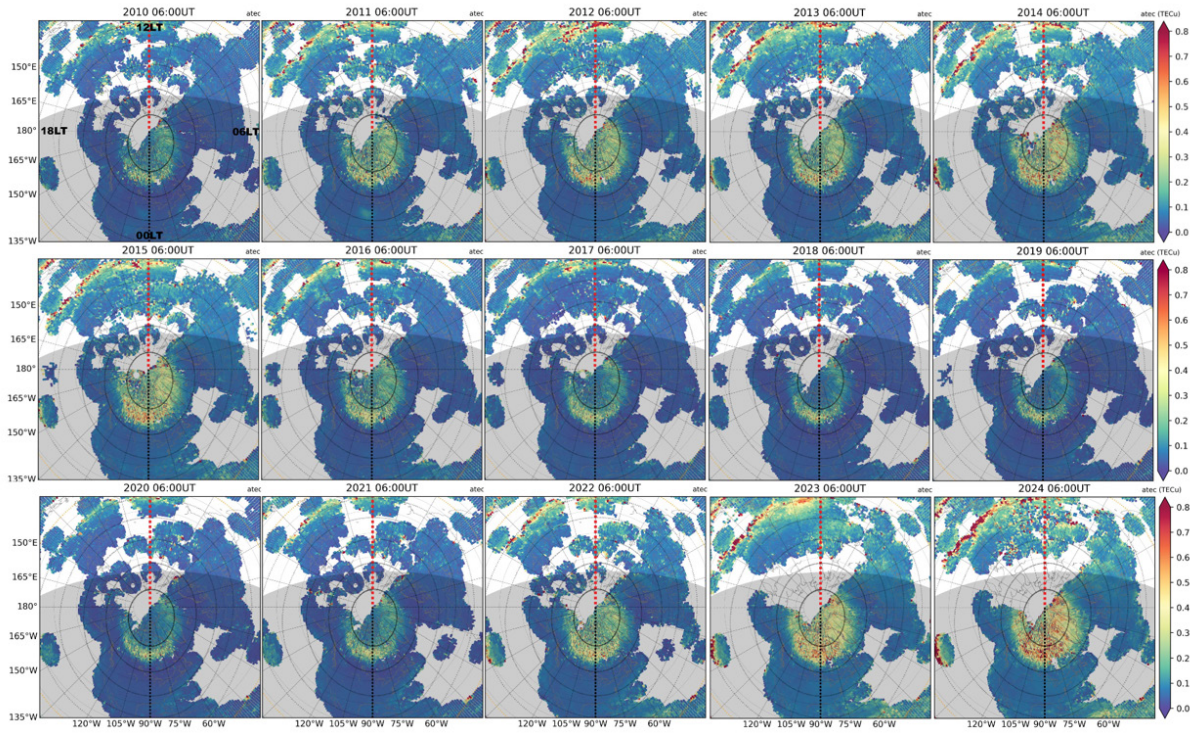
Fig. 15. Northern polar maps at 06 UT as yearly averages for 15 yr from 2010–2024 during those international 10 most quiet days each month. The shadow area represents only solar illumination conditions in January.
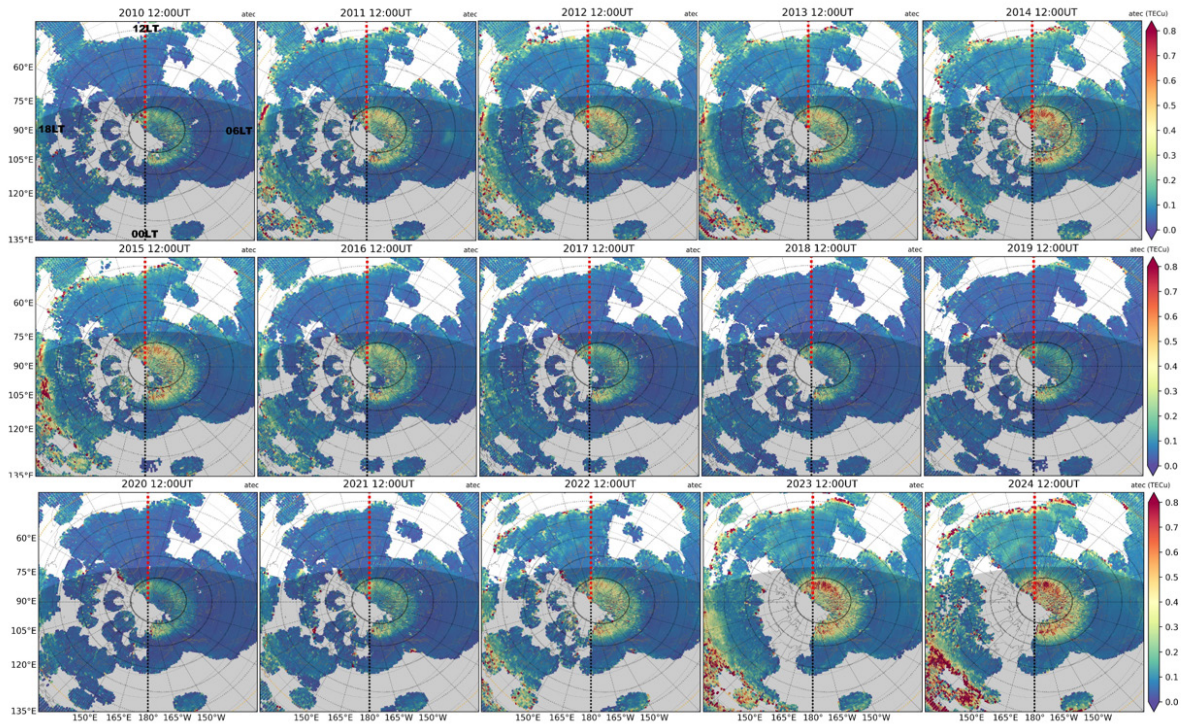

Fig. 16. Northern polar maps at 12 UT as yearly averages for 15 yr from 2010–2024 during those international 10 most quiet days each month. The shadow area represents only solar illumination conditions in January.

mesoscale irregularities, future in-depth analyses are required to quantitatively establish the relationship between the GNSS-measured "irregularity oval" and the auroral oval determined by energetic particle measurements. A subsequent step involves developing a novel GNSS TEC-based "irregularity oval" model that can account for seasonal, magnetic local time, apex latitude, and longitude variations, as well as the dependency on geomagnetic disturbance and solar activity.

ACKNOWLEDGMENTS

ORCIDS

Shun-Rong Zhang
    https://orcid.org/0000-0002-1946-3166
Anthea J. Coster   https://orcid.org/0000-0001-8980-6550
Philips J. Erickson
    https://orcid.org/0000-0002-0031-9324
Larisa P. Goncharenko
    https://orcid.org/0000-0001-9031-7439
Jing Liu   https://orcid.org/0000-0001-6401-6237

REFERENCES

Angelopoulos V, The THEMIS mission, Space Sci. Rev. 141, 5-34. https://doi.org/10.1007/s11214-008-9336-1

Chang H, Kil H, Sun AK, Zhang SR, Lee J, Ionospheric disturbances in low- and midlatitudes during the geomagnetic storm on 26 August 2018, J. Geophys. Res. Space Phys. 127, e2021JA029879 (2022). https://doi.org/10.1029/2021JA029879

Cherniak I, Krankowski A, Zakharenkova I, Observation of the ionospheric irregularities over the Northern Hemisphere: methodology and service, Radio Sci. 49, 653-662 (2014). https://doi.org/10.1002/2014RS005433

Cherniak I, Krankowski A, Zakharenkova I, ROTI maps: a new IGS ionospheric product characterizing the ionospheric irregularities occurrence, GPS Sol. 22, 69 (2018). https://doi.org/10.1007/s10291-018-0730-1

Chou MY, Shen MH, Lin CCH, Yue J, Chen CH, et al., Gigantic circular shock acoustic waves in the ionosphere triggered by the launch of FORMOSAT-5 satellite, Space Weather. 16, 172-184 (2018). https://doi.org/10.1002/2017SW001738

Coster A, Herne D, Erickson P, Oberoi D, Using the Murchison Widefield Array to observe midlatitude space weather, Radio Sci. 47, RS0K07 (2012). https://doi.org/10.1029/2012RS004993

Coster AJ, Goncharenko L, Zhang SR, Erickson PJ, Rideout W, et al., GNSS observations of ionospheric variations during the 21 August 2017 solar eclipse, Geophys. Res. Lett. 44, 12041-12048 (2017). https://doi.org/10.1002/2017GL075774

Ding F, Wan W, Ning B, Wang M, Large-scale traveling ionospheric disturbances observed by GPS total electron content during the magnetic storm of 29–30 October 2003, J. Geophys. Res. Space Phys. 112, A06309 (2007). https://doi.org/10.1029/2006JA012013

Donovan E, Mende S, Jackel B, Frey H, Syrjäsuo M, et al., The THEMIS all-sky imaging array: system design and initial results from the prototype imager, J. Atmos. Sol. Terres. Phys. 68, 1472-1487 (2006). https://doi.org/10.1016/j.jastp.2005.03.027

Ebihara Y, Ejiri M, Simulation study on fundamental properties of the storm-time ring current, J. Geophys. Res. 105, 15843–15859 (2000). https://doi.org/10.1029/1999JA900493.

England SL, Greer KR, Zhang SR, Evans JS, Solomon SC, et al., First comparison of travelling atmospheric disturbances observed in the middle thermosphere by GOLD to travelling ionospheric disturbances seen in ground-based total

electron content observations, J. Geophys. Res. Space Phys. e2021JA029248 (2021). https://doi.org/10.1002/essoar.10506459.1

Evans DS, The observations of a near monoenergetic flux of auroral electrons, J. Geophys. Res. 73, 2315-2323 (1968). https://doi.org/10.1029/JA073i007p02315

Feldstein YI, Starkov GV, Dynamics of auroral belt and polar geomagnetic disturbances, Planet. Space Sci. 15, 209-229 (1967). https://doi.org/10.1016/0032-0633(67)90190-0

Foster JC, Burke WJ, SAPS: a new categorization for sub-auroral electric fields, EOS Trans. Am. Geoohys. Union. 83, 393 (2002). https://doi.org/10.1029/2002EO000289

Foster JC, Coster AJ, Erickson PJ, Holt JM, Lind FD, et al., Multiradar observations of the polar tongue of ionization, J. Geophys. Res. Space Phys. 110, A09S31 (2005). https://doi.org/10.1029/2004JA010928

Frey HU, Mende SB, Carlson CW, Gérard JC, Hubert B, et al., The electron and proton aurora as seen by IMAGE-FUV and FAST. Geophys. Res. Lett. 28, 1135-1138 (2001). https://doi.org/10.1029/2000GL012352

Gjerloev JW, The SuperMAG data processing technique, J. Geophys. Res. Space Phys. 117, A09213 (2012). https://doi.org/10.1029/2012JA017683

Grocott A, Wild JA, Milan SE, Yeoman TK, Superposed epoch analysis of the ionospheric convection evolution during substorms: onset latitude dependence, Ann. Geophys. 27, 591-600 (2009). https://doi.org/10.5194/angeo-27-591-2009

Holzworth RH, Meng CI, Mathematical representation of the auroral oval, Geophys. Res. Lett. 2, 377-380 (1975). https://doi.org/10.1029/GL002i009p00377

Iijima T, Potemra TA, Field-aligned currents in the dayside cusp observed by TRIAD, J. Geophys. Res. 81, 5971-5979 (1976). https://doi.org/10.1029/JA081i034p05971

Inchin PA, Bhatt A, Cummer SA, Eckermann SD, Harding BJ, et al., Multi-layer evolution of acoustic-gravity waves and ionospheric disturbances over the United States after the 2022 Hunga Tonga volcano eruption, AGU Adv. 4, e2023AV000870 (2023). https://doi.org/10.1029/2023AV000870

Jakowski N, Béniguel Y, de Franceschi G, Pajares MH, Jacobsen KS, et al., Monitoring, tracking and forecasting ionospheric perturbations using GNSS techniques, J. Space Weather Space Clim. 2, A22 (2012). https://doi.org/10.1051/swsc/2012022

Kivelson MG, Russell CT, Introduction to Space Physics (Cambridge University Press, Cambridge, UK, 1995).

Lockwood M, Cowley SWH, Ionospheric convection and the substorm cycle, ESA SP-335, ed. Mattock C, (European Space Agency Publications, Nordvijk, 1993), 99-109.

Lu X, Wu H, Heale C, England S, Zhang S, Impacts of thunderstorm-generated gravity waves on the ionosphere-thermosphere

using TIEGCM-NG/MAGIC simulations and comparisons with GNSS TEC, ICON, and COSMIC-2 observations, J. Geophys. Res. Space Phys. 129, e2024JA032854 (2024). https://doi.org/10.1029/2024JA032854

Lyons LR, Nishimura Y, Zhang SR, Coster AJ, Bhatt A, et al., Identification of auroral zone activity driving large-scale traveling ionospheric disturbances, J. Geophys. Res. Space Phys. 124, 700-714 (2019). https://doi.org/10.1029/2018JA025980

Mrak S, Semeter J, Drob D, Huba JD, Direct EUV/X-ray modulation of the ionosphere during the August 2017 total solar eclipse, Geophys. Res. Lett. 45, 3820-3828 (2018). https://doi.org/10.1029/2017GL076771

Mrak S, Semeter J, Nishimura Y, Rodrigues FS, Coster AJ, et al., Leveraging geodetic GPS receivers for ionospheric scintillation science, Radio Sci. 55, e2020RS007131 (2020). https://doi.org/10.1029/2020RS007131

Newell PT, Meng CI, Lyons KM, Suppression of discrete aurorae by sunlight, Nature 381, 766-767 (1996). https://doi.org/10.1038/381766a0

Newell PT, Liou K, Zhang Y, Sotirelis T, Paxton LJ, et al., OVATION Prime-2013: extension of auroral precipitation model to higher disturbance levels, Space Weather, 12, 368–379 (2014). https://doi.org/10.1002/2014SW001056

Nicolls MJ, Heinselman CJ, Three-dimensional measurements of traveling ionospheric disturbances with the Poker Flat Incoherent Scatter Radar, Geophys. Res. Lett. 34, L21104 (2007). https://doi.org/10.1029/2007GL031506

Nishimura Y, Zhang SR, Lyons LR, Deng Y, Coster AJ, et al., Source region and propagation of dayside large-scale traveling ionospheric disturbances, Geophys. Res. Lett. 47, e2020GL089451 (2020). https://doi.org/10.1029/2020GL089451

Pi X, Mannucci AJ, Lindqwister UJ, Ho CM, Monitoring of global ionospheric irregularities using the worldwide GPS network, Geophys. Res. Lett. 24, 2283-2286 (1997). https://doi.org/10.1029/97GL02273

Rideout W, Coster A, Automated GPS processing for global total electron content data, GPS Solut. 10, 219-228 (2006). https://doi.org/10.1007/s10291-006-0029-5

Russell CT, McPherron RL, Semiannual variation of geomagnetic activity, J. Geophys. Res. 78, 92-108 (1973). https://doi.org/10.1029/JA078i001p00092

Saito A, Fukao S, Miyazaki S, High resolution mapping of TEC perturbations with the GSI GPS network over Japan, Geophys. Res. Lett. 25, 3079-3082 (1998). https://doi.org/10.1029/98GL52361

Sato M, Shiokawa K, Oyama S, Otsuka Y, Shinbori A, et al., Statistical analysis of low-latitude boundary of polar-type medium-scale traveling ionospheric disturbances observed

by a 630-nm airglow imager at Nyrölä, Finland, J. Geophys. Res. Space Phys. 129, e2023JA032077 (2024). https://doi.org/10.1029/2023JA032077

Savitzky A, Golay MJE, Smoothing and differentiation of data by simplified least squares procedures, Anal. Chem. 36, 1627-1639 (1964). https://doi.org/10.1021/ac60214a047

Schmidt AL, Meriwether JW, Cooper MB, Gerrard AJ, Goodwin LV, et al., Detection of wave activity in measurements of thermospheric vertical winds and temperatures at subauroral latitudes, Front. Astron. Space Sci. 12, 1613164 (2025). https://doi.org/10.3389/fspas.2025.1613164

Sergeev VA, Angelopoulos V, Nakamura R, Recent advances in understanding substorm dynamics, Geophys. Res. Lett. 39, L05101 (2012). https://doi.org/10.1029/2012GL050859

Shiokawa K, Yumoto K, Kamide Y, High-speed all-sky imaging system for studying auroral dynamics, Opt. Eng. 35, 3602-3608 (1996). https://doi.org/10.1117/1.601116

Sun W, Li G, Zhang SR, Hu L, Dai G, et al., Regional ionospheric super bubble induced by significant upward plasma drift during the 1 December 2023 geomagnetic storm, J. Geophys. Res. Space Phys. 129, e2024JA032430 (2024). https://doi.org/10.1029/2024JA032430

Trop CC, LaBelle J, Erickson PJ, Zhang SR, McGaw D, et al., Tracking traveling ionospheric disturbances through Doppler-shifted AM radio transmissions, Atmos. Meas. Tech. 18, 1909-1925 (2025). https://doi.org/10.5194/amt-18-1909-2025

Tyska J, Deng Y, Zhang S, Lin CY, Ionospheric disturbances generated by the 2015 Calbuco eruption: comparison of GITM-R simulations and GNSS observations, Space Weather. 22, e2023SW003502 (2024). https://doi.org/10.1029/2023SW003502

Vierinen J, Coster AJ, Rideout WC, Erickson PJ, Norberg J, Statistical framework for estimating GNSS bias, Atmos. Meas. Tech. 9, 1303-1312 (2016). https://doi.org/10.5194/amt-9-1303-2016

Xiong C, Lühr H, An empirical model of the auroral oval derived from champ field-aligned current signatures: part 2, Ann. Geophys. 32, 623-631 (2014). https://doi.org/10.5194/angeo-32-623-2014

Xiong C, Lühr H, Wang H, Johnsen MG, Determining the boundaries of the auroral oval from champ field-aligned current signatures: part 1, Ann. Geophys. 32, 609-622 (2014). https://doi.org/10.5194/angeo-32-609-2014

Zakharenkova I, Astafyeva E, Cherniak I, GPS and GLONASS observations of large-scale traveling ionospheric disturbances during the 2015 St. Patrick's Day storm, J. Geophys. Res. Space Phys. 121, 12138-12156 (2016). https://doi.org/10.1002/2016JA023332

Zhang QH, Ma YZ, Jayachandran PT, Moen J, Lockwood M, et al., Polar cap hot patches: enhanced density structures different from the classical patches in the ionosphere, Geophys. Res. Lett. 44, 8159-8167 (2017a). https://doi.org/10.1002/2017GL073439

Zhang QH, Zhang BC, Lockwood M, Hu HQ, Moen J, et al., Direct observations of the evolution of polar cap ionization patches, Science. 339, 1597-1600 (2013). https://doi.org/10.1126/science.1231487

Zhang SR, Coster AJ, Erickson PJ, Goncharenko LP, Rideout W, et al., Traveling ionospheric disturbances and ionospheric perturbations associated with solar flares in September 2017, J. Geophys. Res. Space Phys. 124, 5894-5917 (2019a). https://doi.org/10.1029/2019JA026585

Zhang SR, Erickson PJ, Coster AJ, Rideout W, Vierinen J, et al., Subauroral and polar traveling ionospheric disturbances during the 7–9 September 2017 storms, Space Weather. 17, 1748-1764 (2019b). https://doi.org/10.1029/2019SW002325

Zhang SR, Erickson PJ, Gasque LC, Aa E, Rideout W, et al., Electrified postsunrise ionospheric perturbations at Millstone Hill, Geophys. Res. Lett. 48, e2021GL095151 (2021). https://doi.org/10.1029/2021GL095151

Zhang SR, Erickson PJ, Goncharenko LP, Coster AJ, Rideout W, et al., Ionospheric bow waves and perturbations induced by the 21 August 2017 solar eclipse, Geophys. Res. Lett. 44, 12067-12073 (2017b). https://doi.org/10.1002/2017GL076054

Zhang SR, Nishimura Y, Erickson PJ, Aa E, Kil H, et al., Traveling ionospheric disturbances in the vicinity of Storm Enhanced Density at midlatitudes, J. Geophys. Res. Space Phys. 127, e2022JA030429 (2022). https://doi.org/10.1029/2022JA030429

Zhang SR, Nishimura Y, Vierinen J, Lyons LR, Knipp DJ, et al., Simultaneous global ionospheric disturbances associated with penetration electric fields during intense and minor solar and geomagnetic disturbances, Geophys. Res. Lett. 50, e2023GL104250 (2023). https://doi.org/10.1029/2023GL104250

Zhang Y, Paxton LJ, An empirical Kp-dependent global auroral model based on TIMED/GUVI FUV data, J. Atmos. Sol. Terres. Phys. 70, 1231-1242 (2008). https://doi.org/10.1016/j.jastp.2008.03.008

Zou S, Moldwin MB, Ridley AJ, Nicolls MJ, Coster AJ, et al., On the generation/decay of the storm-enhanced density plumes: role of the convection flow and field-aligned ion flow, J. Geophys. Res. Space Phys. 119, 8543-8559 (2014). https://doi.org/10.1002/2014JA020408

Zou S, Perry GW, Foster JC, Recent Advances in Polar Cap Density Structure Research, in Ionosphere Dynamics and Applications, eds. Huang C, Lu G, Zhang Y, Paxton LJ (American Geophysical Union (AGU), 2021), 67-82.